

1 **Preliminary analysis of the performance of the Landsat 8/OLI land surface**
2 **reflectance product**

3
4 Eric Vermote¹, Chris Justice², Martin Claverie^{2,1}, Belen Franch^{2,1}
5

6 ¹NASA/GSFC Code 619, Greenbelt, MD, USA
7 ²University of Maryland, Dept. of Geographical Sciences, College Park, MD, USA
8

9 **Abstract**

10
11 The surface reflectance, i.e., satellite derived top of atmosphere (TOA) reflectance
12 corrected for the temporally, spatially and spectrally varying scattering and absorbing
13 effects of atmospheric gases and aerosols, is needed to monitor the land surface reliably.

14 For this reason, the surface reflectance, and not TOA reflectance, is used to generate the
15 greater majority of global land products, for example, from the Moderate Resolution
16 Imaging Spectroradiometer (MODIS) and Visible Infrared Imaging Radiometer Suite
17 (VIIRS) sensors. Even if atmospheric effects are minimized by sensor design,
18 atmospheric effects are still challenging to correct. In particular, the strong impact of
19 aerosols in the Visible and Near Infrared spectral range can be difficult to correct,
20 because they can be highly discrete in space and time (e.g., smoke plumes) and because
21 of the complex scattering and absorbing properties of aerosols that vary spectrally and
22 with aerosol size, shape, chemistry and density.

23
24 This paper presents the Landsat 8 Operational Land Imager (OLI) atmospheric correction
25 algorithm that has been developed using the Second Simulation of the Satellite Signal in
26 the Solar Spectrum Vectorial (6SV) model, refined to take advantage of the narrow OLI
27 spectral bands (compared to Thematic Mapper/Enhanced Thematic Mapper
28 (TM/ETM+)), improved radiometric resolution and signal-to-noise. In addition, the
29 algorithm uses the new OLI Coastal aerosol band (0.433–0.450 μ m), which is particularly

30 helpful for retrieving aerosol properties, as it covers shorter wavelengths than the
31 conventional Landsat, TM and ETM+ blue bands. A cloud and cloud shadow mask has
32 also been developed using the “cirrus” band (1.360–1.390 μm) available on OLI, and the
33 thermal infrared bands from the Thermal Infrared Sensor (TIRS) instrument. The
34 performance of the surface reflectance product from OLI is analyzed over the Aerosol
35 Robotic Network (AERONET) sites using accurate atmospheric correction (based on in
36 situ measurements of the atmospheric properties), by comparison with the MODIS
37 Bidirectional Reflectance Distribution Function (BRDF) adjusted surface reflectance
38 product and by comparison of OLI derived broadband albedo from United States Surface
39 Radiation Budget Network (US SURFRAD) measurements.

40

41

42 **1. Introduction**

43

44 The need for standard products was recognized early in the National Aeronautics and

45 Space Administration (NASA) Earth Observation Satellite (EOS) program and

46 considerable resources have been allocated for the generation of geophysical products.

47 The objective being, to take away the burden of data processing from the user community

48 and facilitate uptake of the data by modelers and operational users. For the MODIS, three

49 suites of geophysical peer-reviewed products were developed in the areas of vegetation

50 parameterization, energy balance and land cover and change (Justice and Townshend

51 2002). Several of these MODIS products are derived using the Surface Reflectance

52 product.

53 Atmospheric effects introduce a non-negligible perturbation to the reflectance observed

54 by Landsat TM. This perturbation depends on the wavelength, the geometry of

55 illumination and observation, and the concentration of aerosols and gases at a given time

56 and location. In the visible part of the Spectrum, aerosols dominates and at longer

57 wavelengths water vapor can greatly absorb radiation in specific regions. This

58 perturbation can easily reach up to 15% relative and 0.05 unit of reflectance for the TM

59 (Vermote et al., 1997a). Even for comparative studies that do not retrieve biophysical

60 parameters, atmospheric correction should be applied to prevent changes due to

61 atmospheric effects being interpreted as changes in the surface conditions.

62

63 A number of atmospheric correction methodologies have been developed but those using

64 radiative transfer algorithms and atmospheric characterization data provide the greatest

65 potential for automated large area application. The approach proposed here is a

66 physically based atmospheric correction technique that aims at producing the reflectance

67 that would be measured at ground level if there were no atmosphere. However, it is
68 limited to uniform and flat targets. For heterogeneous landscapes, adjacency effects can
69 be corrected in a subsequent step that is computationally expensive and will only improve
70 the quality of the product under specific conditions (Vermote, 2003) and as a result, this
71 correction is not performed operationally. For rugged terrain, topographic effects can
72 introduce important artifacts if not accounted for (Tan et al., 2013) but can also be
73 corrected after standard atmospheric correction and will not be discussed in this paper.
74 Such an approach has been applied to MODIS since 2000 to generate daily and 8-day
75 surface reflectance products. It is based on a rigorous radiative transfer model, the
76 vectorial version of the 6S code (Vermote et al. 1997b, Kotchenova et al. 2006), a
77 description of the atmosphere properties based on ancillary data for the less critical part
78 of the atmospheric constituents (i.e. Rayleigh scattering, gaseous absorption) and on
79 retrieval of the aerosol concentration using the bands centered at the shortest wavelengths
80 (blue) where the surface reflectance is generally small and the aerosol signal is strong.
81 A similar approach has been successfully applied to Landsat data in the operational
82 environment of the Landsat Ecosystem Disturbance Adaptive Processing System
83 (LEDAPS) Project where a version of the algorithm has been implemented, tested,
84 validated and widely distributed (Masek et al., 2006). Application to Landsat has
85 demonstrated a performance comparable to the MODIS algorithm for the aerosol
86 retrieval over land, when compared to AERONET, with a one sigma uncertainty lower
87 than $0.05+0.2\text{AOT}$ (where AOT stands for Aerosol Optical Thickness) (Masek et al.
88 2006, Remer et al. 2005) as well as for the surface reflectance product (Claverie et al.,
89 2015). For Landsat 8/OLI, the recent developments and improvements of MODIS surface
90 reflectance Collection 6 were implemented, taking advantage of the improved

91 radiometric performance and spectrally narrow bands located at wavelengths that are less
92 subject to atmospheric absorption, as well as using better ancillary datasets (Section 2).
93 The improvements translated into enhanced performance in terms of accuracy, precision
94 and uncertainty metrics of the Landsat8/OLI surface reflectance, as compared to its
95 precursors (Landsat 7/ETM+ and 5/TM) and as shown by the comparison with the
96 reference dataset obtained over AERONET sites (Section 3.1). The accuracy of the
97 surface reflectance was further assessed by inter-comparison with the MODIS Surface
98 Reflectance product (Section 3.2) and by comparing a Landsat 8 derived broadband
99 albedo to US SURFRAD network measurements (Section 3.3.).

100

101

102

103 **2. Methodology**

104

105

106 **2.1. Surface reflectance inversion / atmospheric correction**

107

108 The method adopted for atmospheric correction relies on the inversion of the relatively
109 simple equation in the Lambertian case, with no adjacency effects that account for a
110 simplified coupling of the absorption by atmospheric gases and scattering by molecules
111 and aerosols as it is implemented in the 6SV radiative transfer code (Vermote et al.
112 1997b, Kotchenova et al. 2006):

$$\rho_{TOA}(\theta_s, \theta_v, \varphi, P, \overbrace{\tau_A, \omega_0, P_A}^{Aer}, U_{H_2O}, U_{O_3}) = Tg_{OG}(m, P) Tg_{O_3}(m, U_{U_{O_3}}) \left[\rho_{atm}(\theta_s, \theta_v, \varphi, P, Aer, U_{H_2O}) + \right. \\ \left. Tr_{atm}(\theta_s, \theta_v, P, Aer) \frac{\rho_s}{1 - S_{atm}(P, Aer) \rho_s} Tg_{H_2O}(m, U_{U_{H_2O}}) \right] \quad [1a]$$

114 where

115 ρ_{TOA} is the reflectance at the top of the atmosphere, ρ_{atm} is the atmosphere intrinsic
116 reflectance, Tr_{atm} is the total atmosphere transmission (downward and upward), S_{atm} is the
117 atmosphere spherical albedo, and ρ_s is the surface reflectance to be retrieved by the
118 atmospheric correction procedure:

119 the geometric conditions are described by the solar zenith angle θ_s , the view zenith angle
120 θ_v , and the relative azimuth ϕ (or the difference between the solar and view azimuth
121 angles);

122 P is the pressure that influences the number of molecules and the concentration of
123 absorbing gases in the atmosphere, Tg designates the gaseous transmission by water
124 vapor (Tg_{H_2O}), ozone (Tg_{O_3}), or other gases (Tg_{OG}), U_{H_2O} is the integrated water vapor

125 content, U_{O_3} is the integrated ozone content, and m is the so-called “air-mass” computed
126 as $1/\cos(\theta_s) + 1/\cos(\theta_v)$;

127 τ_A , ω_0 and P_A describe the aerosol properties and are spectrally dependent: τ_a is the
128 aerosol optical thickness, ω_0 is the aerosol single scattering albedo, and P_A is the aerosol
129 phase function.

130 Equation [1a] is a modified form of the original equation of transfer for a lambertian
131 uniform target of reflectance ρ_s :

$$132 \quad \rho_{TOA} = \rho_{atm} + Tr_{atm} \frac{\rho_s}{1 - S_{atm} \rho_s} \quad [1b]$$

133 Equation [1b] is valid under all conditions but the computation of the atmospheric terms
134 in the equation necessitate a radiative transfer code that has limitations. The main
135 limitation of 6SV is the plane parallel assumption for the atmosphere, which limits the
136 quoted accuracy (0.4%) to Sun and view zenith angles lower than 75 degrees. In addition
137 to this limitation, Equation [1a] supposes that scattering and absorption could be
138 decoupled, which is not true where both strong absorption and scattering regimes occur
139 ,for example near strong water vapor absorption lines in the near-infrared (e.g. in MODIS
140 band 18 and 19).

141 So for Landsat 8 bands 1 to 8, the effect of water vapor on the atmosphere intrinsic
142 reflectance can be approximated as:

$$143 \quad \rho_{atm}(\theta_s, \theta_v, \phi, P, Aer, U_{H_2O}) = \rho_R(\theta_s, \theta_v, \phi, P) + \\ (\rho_{R+Aer}(\theta_s, \theta_v, \phi, P, Aer) - \rho_R(\theta_s, \theta_v, \phi, P)) \Gamma g_{H_2O}(m, \frac{U_{H_2O}}{2}) \quad [2]$$

144 where ρ_R represents the reflectance of the atmosphere due to molecular (Rayleigh)
145 scattering and ρ_{R+Aer} represents the reflectance of the mixture of molecules and aerosol

146 particles. Accounting correctly for the mixing and the so-called coupling effect [2] is
147 important for achieving a high accuracy of atmospheric effect modeling. This
148 approximation conserves the correct computation of the coupling and assumes that water
149 vapor is mixed with aerosol particles and that molecular scattering is not affected by
150 water vapor absorption. It should be noted that Equation [2] represents an average case
151 where we consider that half of the water vapor present in the atmosphere absorbs the
152 aerosol path radiance. Two additional extreme cases are computed by 6SV, the water
153 vapor above the aerosol layer (maximum absorption) and the water vapor under the
154 aerosol layer (minimum absorption) (Vermote et al. 1997b). These additional cases could
155 be used in the error budget computation.

156 Figure 1 shows a visual illustration of the inversion of Equation [1a], the left side of the
157 figure corresponds to the top of the atmosphere reflectance (the term ρ_{TOA} on the left side
158 of equation [1a]) in OLI band 4,3 and 2 displayed as a RGB color composite, whereas the
159 right side corresponds to the same bands but using the surface reflectance (the term ρ_s
160 inside Equation [1a]).

161

162 As the scheme of the atmospheric correction is relatively simple in terms of input and
163 inversion (see Equation [1a]), the challenge lies in estimating the atmospheric parameters
164 of Equation [1a] and [2].

165 The atmospheric pressure \mathbf{P} is obtained from a combination of data available from a
166 coarse-resolution (one deg., six hours time step) weather prediction model available from
167 NCEP GDAS (2015), sea level pressure P_{sl} and the altitude \mathbf{z} [km] given by a Digital
168 Elevation Model at 0.05 degree resolution (ETOPO5, 1988) and computed as:

169

170
$$P = P_{sl} e^{-z/8}$$

[3]

171 The pressure should be representative of the average atmospheric pressure along the path
172 from the Sun to the target and back to the satellite for primary scattering, and along a
173 even more complicated path for multiple scattering. Given the fact the Sun is usually not
174 at nadir but more often at 45 degree on average and that the height of the atmosphere is
175 about 10km, the resolution used in the pressure field should be about 10km on average.
176 That is why using a spatial resolution much higher than a few kilometers is not needed
177 nor desirable. In practice the pressure at sea level is taken directly from the MODIS Terra
178 ancillary information already re-gridded at 0.05 degree at the time of overpass of Terra
179 (approximately 10:30AM).

180 The ozone amount UO_3 is obtained via NCEP GDAS (2015) (at 1deg., 6 hours time step)
181 via the ancillary information included in the MODIS surface reflectance Climate
182 Modeling Grid (MOD09CMA). The surface reflectance Climate Modeling Grid (CMG)
183 adopted a simple Geographic latitude/longitude projection at 0.05 degree (~ 5.5 km).

184
185 The water vapor is also extracted from the ancillary information included in the MODIS
186 surface reflectance Climate Modeling Grid (MOD09CMA) for Terra, which is itself
187 computed from the MODIS near-infrared band 18 (931-941 nm) and 19 (915-965 nm) at
188 1 km spatial resolution (Gao and Kaufman, 2003). Using the MODIS derived water vapor
189 is preferred to using the GDAS data for two reasons (i) the high spatial and temporal
190 variability of water vapor (a couple of hours and a few tens of kilometers) compared to
191 ozone for example (days and a hundred of kilometers) (ii) the established good
192 performance of the MODIS water vapor retrieval (5 to 10% errors) (Gao and Kaufman,
193 2003). This however assumes that MODIS water vapor retrieval is possible, as it requires

194 cloud free conditions. The assumption is that cloud distribution is the same for Landsat
195 and MODIS Terra which might not be the case and will necessitate further improvement
196 of the ancillary dataset (e.g. using GDAS in lieu of MODIS over cloudy pixels).
197 The aerosol characteristics (τ_A , ω_0 and P_A) pose a greater challenge. The problem is first
198 simplified by assuming a standard dynamic aerosol model, “Urban Clean” which was the
199 model proposed by Dubovik in his analysis of the AERONET results (Dubovik et al.,
200 2002). The choice of this aerosol model worldwide is due to the limited number of bands
201 available to attempt a model inversion and the relatively preliminary nature of the OLI
202 surface reflectance product. Then the aerosol optical thickness is inverted using the two
203 blue bands available on Landsat8/OLI (band 1 and 2) for each non-water pixel that has
204 not been flagged as cirrus. The inversion scheme is adapted from the MODIS Collection
205 6 surface reflectance algorithm, which is based on the Collection 5 algorithm and stems
206 from the work of Kaufman et al., (1997). The basic principle of this method was to use an
207 a-priori relationship between the reflectance observed in the middle infra-red (mid-IR)
208 ($2.1\mu\text{m}$) and the blue ($0.47\mu\text{m}$) and Red ($0.66\mu\text{m}$) bands of MODIS to constrain the
209 inversion. That relationship is connected by the fact that the vegetation liquid water
210 content that influences the signal in the mid-IR is related to the photosynthetic activity
211 that absorbs the radiation in the blue and red. However, both the MODIS aerosol group
212 (see Figure 1 of Levy et al., 2007), and the MODIS surface reflectance group (Vermote
213 and Saleous, 2006, Vermote and Kotchenova, 2008) found that there was a stronger
214 relationship between red and blue MODIS bands than the blue and mid-IR.
215 Consequently, the approach implemented in MODIS Collection 6 and the current version
216 of LEDAPS surface reflectance use the relationship between the blue and red band to
217 invert AOT. This approach is naturally the one used for this first version of the

218 Landsat8/OLI surface reflectance product and the details of the implementation are given
219 in the next section.

220
221

222 **2.2. Landsat 8/OLI aerosol optical thickness inversion**

223

224 The method for inverting the AOT from OLI is relatively simple if the ratio between the
225 red and blue bands of OLI can be known for every 30m pixel (Figure 3c). First, this ratio
226 is computed at coarse resolution (0.05 degree) from 10 years of MODIS (Terra) and
227 MISR data (see Figure 2). The MISR AOT product is used as input to the atmospheric
228 correction of the MODIS TOA data for each valid observation, providing the MODIS
229 surface reflectances that can be used to derive a ratio at 0.05 degree. The data are
230 carefully filtered for clouds and high AOT values. This data processing enables one to
231 account for the accuracy of that ratio globally and across several years and seasons. The
232 ratio is computed for each valid observation and subsequently fitted as a linear function
233 of $NDVI_{MIR}$ (Figure 3b), a vegetation index that uses the Mid-IR (2.1 μ m) channel instead
234 of Red:

235

236
$$NDVI_{MIR} = \frac{NIR - MidIR/2}{NIR + MidIR/2} \quad [4]$$

237 The advantage of this index is that it is much less sensitive to aerosols because of the use
238 of Mid-IR in lieu of red but still close to the original NDVI as the Mid-IR and red ratio is
239 around 0.5 over most surfaces (See Levy et al. 2007).

240

241 Second, this parameterization of the ratio as a function of $NDVI_{MIR}$ at the CMG level in
242 addition to capturing the potential seasonal/annual variability of the ratio, enables one to
243 scale this quantity down to the spatial resolution of OLI and use it in the retrieval of AOT

244 at the OLI pixel level (Figure 3c). In addition to retrieving the AOT for each OLI pixel, a
245 measure of the goodness of inversion is provided by computing the inversion “residual”
246 using the two blue bands available on OLI (band 1 and 2) as:

247

248
$$Residual = \sqrt{\frac{(\rho_s^1 - r_{1,4}\rho_s^4)^2 + (\rho_s^2 - r_{2,4}\rho_s^4)^2}{2}} \quad [5]$$

249 where ρ_s^1 , ρ_s^2 and ρ_s^4 are the surface reflectance in OLI band 1,2,4 derived using the
250 AOT inverted using red (band 4) and blue (band 1) and $r_{1,4}$ (resp. $r_{2,4}$) is the ratio
251 between band 1 (resp. band 2) and band 4 of OLI.

252 This residual turned out to be very useful to detect clouds, as in the case of thick clouds,
253 either the inversion did not converge or the residual was very high. A threshold as a
254 function of the AOT retrieved was set to screen all the inversions for which the residual
255 exceeded $0.005 + 0.05AOT$, in that case further testing was done to investigate cloud
256 contamination. Figure 3d illustrates a detail of a scene from Missoula, Montana which
257 shows how the residual can indeed catch some of the most obvious cloud in the image
258 (also shown is the cirrus band).

259 After cloud and cloud shadow masking, residual and water masking is performed. Then, a
260 gap filling process is performed using all valid AOT values. This gap filling process is
261 implemented within an initial window of 10x10 pixels, which is grown by a factor 2 until
262 all the pixels in the image have a valid AOT. At each step the pixels within this window
263 with no valid AOT retrieval are filled with the average of the valid AOT and flagged
264 accordingly.

265

266 **3. Validation**

267
268 The direct validation of land surface reflectance is problematic since there are no
269 systematic measurements at the adequate spatial and spectral resolution that could be
270 used as it is the case for example for validating aerosol optical thickness (AERONET).
271 Recognizing this problem, we have adopted, as many others, an indirect approach using
272 three different sources of information to validate the Landsat8/OLI surface reflectance
273 product: (i) The AERONET data associated with a accurate radiative transfer code, (ii)
274 the MODIS surface reflectance product adjusted for BRDF effect and spectral differences
275 with OLI, (iii) the SURFRAD measurements of the shortwave albedo over five different
276 sites. The details of each analysis are given hereafter.

277

278 **3.1. Assessment of the performance of the Landsat 8/OLI surface reflectance**
279 **product using AERONET data.**

280
281 Key steps in developing a science quality, long-term dataset are establishing the pre and
282 post-launch uncertainty estimates and validating the product. In addition to tracking the
283 calibration of the sensor, which is seminal to the atmospheric correction, the current
284 approach relied first on the validation of the radiative transfer approach (Kotchenova et
285 al. 2006,2008; Kotchenova and Vermote, 2007), validating the 6SV code by inter-
286 comparison with other codes, including the unambiguous Monte Carlo approach
287 (Kotchenova et al., 2006 which shows 6SV to agree within 0.4% of the Monte Carlo
288 results, <http://rtcodes.ltdri.org/>) and the application of the radiative transfer code over
289 sites with detailed descriptions of the atmospheric properties from the AERONET
290 (Holben et al., 1998). This allowed us to retrieve very accurate reflectance standards,
291 such as measurements of water reflectance from MOBY off the coast of Lanai Island,
292 Hawaii (Kotchenova et al. 2006). Once the radiative transfer approach is established, a

293 practical means of validation is to establish a reference dataset based on the best possible
294 atmospheric correction of the data of interest. In practice, the full radiative transfer code,
295 6SV, is used and not the look up tables and parameterization of the gaseous transmission
296 used in the operational surface reflectance product of any sensor. The best possible
297 source of water vapor and aerosol information is used as input to the code, which is
298 achieved whenever two valid AERONET observations that bracket the satellite data
299 within 15 minutes can be obtained. This reference dataset can then be used to determine
300 the accuracy, precision and uncertainty (APU) of the surface reflectance product
301 originally defined by the National Polar-Orbiting Operational Environmental Satellite
302 System (NPOESS) project to evaluate a variety of Earth Data Records (EDR) and are
303 computed as follows:

$$304 A = \frac{\sum_{i=1}^N (\mu_i^e - \mu_i^t)}{N} \quad [6]$$

$$305 P^2 = \frac{\sum_{i=1}^N (\mu_i^e - \mu_i^t - A)^2}{N-1} \quad [7]$$

$$306 U^2 = \frac{\sum_{i=1}^N (\mu_i^e - \mu_i^t)^2}{N} \quad [8]$$

307 Where in this case, μ^e is the operational surface reflectance of the sensor considered and
308 μ^t is the surface reflectance ‘truth’.

309
310 This type of analysis has been undertaken on a global sample basis for the MODIS
311 Surface Reflectance products and Vegetation Indices, as well as for VIIRS (Vermote et
312 al., 2014). It has also been performed for previous Landsat products such as the WELD
313 (Roy et al., 2010) and the LEDAPS (Masek et al., 2006) products over CONUS (Ju et al.

314 2012). Figure 4 shows the unambiguous conclusions that could be derived from such
315 statistical metrics. The top left of figure 4 is the APU for the top of the atmosphere
316 reflectance observed in the red (0.66 μ m), whereas the top right, bottom left and bottom
317 right are APU for the surface reflectance for LEDAPS, WELD and Landsat 8. The
318 magenta line on each quadrant is the specified uncertainty based on a conservative error
319 budget derived for MODIS (Vermote and Saleous, 2006). From figure 4, one can clearly
320 see that the top of the atmosphere uncertainty (blue curve) exceeds the specification
321 mainly because of a large bias (accuracy, red curve), whereas LEDAPS and WELD for
322 Landsat 7/ETM+ meet the MODIS specification. The WELD product is slightly better
323 than the LEDAPS but necessitates the MODIS aerosol product as input, but the
324 LANDSAT 8 newly developed surface reflectance that uses the previously described
325 aerosol inversion (section 2.2) shows even better performance. Figures 5a-b confirm the
326 good performance of the Landsat 8/OLI surface reflectance product across almost all
327 bands. Also shown is the good performance of the Normalized Difference Vegetation
328 Index (NDVI) derived from the Surface Reflectance band 4 and 5, which have shown to
329 be sensitive to atmospheric effects when using top of the atmosphere reflectance (Justice
330 et al., 1991).

331 Those results only indicate preliminary performances of the OLI surface reflectance
332 product as the dataset used are limited to a relatively modest number of AERONET sites
333 and the selection of the data followed strictly the MODIS protocol in term of rejecting
334 high aerosol cases. A first step forward for a meaningful comparison will be to use the
335 same AERONET selection as a reference as was done by Ju et al., (2012). The
336 complexity in the present case is that we are not only looking at two different algorithms
337 but also two different instruments. To complement this preliminary estimate, results

338 across all bands with the addition of the performance estimates for TM/ETM+ from
339 (Claverie et al., 2015 and Ju et al., 2012) are provided in Table 1, showing that the OLI
340 surface reflectance performances are either close or better than the precursor surface
341 reflectance products. This needs to be confirmed over a larger dataset comparable to the
342 one used by Claverie et al., (2015).

3.2 Inter-comparison with MODIS

The previous section illustrated the validation that can be achieved using AERONET sites. Although robust, this validation is limited to coincident observations and given the relatively low revisit frequency of Landsat 8 (16 days) leads to 71 cases where the comparison was possible. Figure 6 gives an overview of the spatial distribution of those cases (yellow squares). In order to increase the sample, an alternative approach is to inter-compare the Landsat 8/OLI surface reflectance with an already validated product, here the MODIS Aqua Surface Reflectance. Figure 6 shows (red squares) the OLI scenes selected for inter-comparison. The details of the inter-comparison procedure developed for Landsat 5/TM and Landsat 7/ETM+ LEDAPS products involve the normalization of the surface reflectance for directional effects and some basic filtering on the atmospheric conditions (eliminate high aerosol). This approach accounts for spectral band differences between OLI and MODIS and it also involves a spatial aggregation of both datasets to a 0.05 degree grid, limiting the MODIS and OLI collocation error. Details concerning the inter-comparison methodology can be found in Claverie et al. (2015).

359 More importantly, it should be noted that the “error” observed in this inter-comparison is
360 a combination of errors in both the surface reflectance product (MODIS and OLI), as
361 well as residuals from the spectral and directional effect normalization. In this case, we
362 have compared the data to those from Aqua (although band 6 is not compared because of
363 several detector problems with Aqua) because it was found that the geometry of
364 observation was closer between Aqua and OLI than for Terra and OLI, therefore the
365 noise from the directional correction was smaller. The results are presented in Figure 7;
366 the correlation between two dataset is high and the accuracy (bias) might be largely due
367 to spectral and BRDF residuals (1 to 5% across all the bands); the precision is mostly

368 around 5% but is largest in the blue (OLI band 2, MODIS band 3) consistent with the
369 decreased performance of both reflectance products at those wavelengths. Overall, the
370 inter-comparison did not point out any problems with the OLI products that can't be
371 explained by the limitations of such an approach (the BRDF residual noise, for example
372 has been shown to be around 5% (Bréon and Vermote, 2012 and Bréon et al., 2015).

373 Table 2 summarizes the same analysis performed with TM and ETM+, by comparing
374 LEDAPS surface reflectance to Aqua from (Claverie et al., 2015) and confirms the good
375 performance of OLI especially in the visible, where the aerosol effect dominates.

376

377 **3.3 Landsat 8/OLI – MODIS Shortwave Albedo product performance**
378
379 As in the previous section, the goal of this section is to provide additional evidence of the
380 performance of the Landsat 8/OLI surface reflectance product by looking at downstream
381 products that could be in turn be compared to independent “truth”. The Landsat class of
382 sensors by themselves could not derive albedo, which by definition necessitates the
383 integration of several different viewing geometries. However, the Albedo can be
384 estimated using MODIS by the inversion of the Bidirectional Reflectance Distribution
385 Function model (Schaaf et al., 2002). By combining MODIS BRDF information and
386 Landsat data and spatially disaggregating the coarse resolution information, one can
387 derive a reasonable estimate of a Landsat spatial scale Broadband Albedo, as shown by
388 several authors by comparison to flux tower measurements (Shuai et al., 2011, Franch et
389 al., 2014). The Franch et al., (2014) algorithm derives a Landsat surface albedo based on
390 the BRDF parameters estimated from the MODerate Resolution Imaging
391 Spectroradiometer (MODIS) Climate Modeling Grid (CMG) surface reflectance product
392 (M{O,Y}D09) using the VJB method (Vermote, Justice, & Bréon, 2009). The algorithm
393 uses a Landsat unsupervised classification to disaggregate the BRDF parameters to the
394 Landsat spatial resolution. In this section, the method of Franch et al., (2014) is directly
395 applied to both Landsat 8/OLI and Landsat 5 and 7/ETM+ dataset over five SURFRAD
396 sites (i.e. Desert Rock, Table Mountain, Bondville, Goodwin Creek and Penn State
397 University). The results are presented in Figures 8a-b. Figure 8a is taken directly from
398 Franch et al., (2014) where it is shown that using AERONET aerosol data in the
399 atmospheric correction, among other factors can provide a better broadband albedo from
400 Landsat 5/7. Figure 8b shows that even without AERONET data Landsat 8 achieves

401 slightly better performance, although it must be recognized that this validation study
402 should be extended to more cases in the future, as the Landsat 8 archive grows.

403

404 **4. Conclusion**

405

406 This paper described an approach for atmospheric correction of Landsat 8 that takes
407 advantage of the improved sensor characteristics, the latest development in the state of
408 the art of atmospheric correction (MODIS Collection 6), that is traceable and associated
409 with a strong validation background (NASA EOS heritage). The results presented clearly
410 show an improvement of Landsat 8 surface reflectance product over the ad-hoc Landsat
411 5/7 LEDAPS product. Indubitably, this effort will be a corner-stone in a series of science
412 products based on the Landsat class of sensors. This method would also be applicable to
413 European Sentinel 2 sensor (Drusch et al., 2012).

414

415 **Acknowledgement:** This work was supported by NASA grant NNX12AP82G.

416

417

418 **5. References**

419

420

421 Bréon, F. M., & Vermote, E. (2012). Correction of MODIS surface reflectance time
422 series for BRDF effects. *Remote Sensing of Environment*, 125, 1-9.

423

424 Bréon, F.-M.; Vermote, E., Murphy, E.F. & Franch, B. (2015). Measuring the Directional
425 Variations of Land Surface Reflectance From MODIS. *IEEE Transactions on Geoscience*
426 and *Remote Sensing*, 53 (8), 4638-4649.

427

428 Claverie, M., Vermote, E.F., Franch, B. & Masek, J.G., 2015. Evaluation of the Landsat-
429 5 TM and Landsat-7 ETM+ surface reflectance products. *Remote Sensing of*
430 *Environment*, 169, 390-403.

431

432 ETOPO5, Data Announcement 88-MGG-02, Digital relief of the Surface of the Earth.
433 NOAA, National Geophysical Data Center, Boulder, Colorado, 1988.

434

435 Dubovik, O., Holben, B., Eck, T. F., Smirnov, A., Kaufman, Y. J., King, M. D., ... &
436 Slutsker, I. (2002). Variability of absorption and optical properties of key aerosol types
437 observed in worldwide locations. *Journal of the atmospheric sciences*, 59(3), 590-608.

438

439 Franch, B., Vermote, E. F., & Claverie, M. (2014). Intercomparison of Landsat albedo
440 retrieval techniques and evaluation against in situ measurements across the US
441 SURFRAD network. *Remote Sensing of Environment*, 152, 627-637.

442

443 Gao, B. C., & Kaufman, Y. J. (2003). Water vapor retrievals using Moderate Resolution
444 Imaging Spectroradiometer (MODIS) near-infrared channels. *Journal of Geophysical*
445 *Research: Atmospheres (1984–2012)*, 108(D13).

446

447 Ju, J., Roy, D. P., Vermote, E., Masek, J., & Kovalskyy, V. (2012). Continental-scale
448 validation of MODIS-based and LEDAPS Landsat ETM+ atmospheric correction
449 methods. *Remote Sensing of Environment*, 122, 175-184.

450

451 Justice, C. O., Eck, T. F., Tanre, D., & Holben, B. N. (1991). The effect of water vapour
452 on the normalized difference vegetation index derived for the Sahelian region from
453 NOAA AVHRR data. *International Journal of Remote Sensing*, 12(6), 1165-1187.

454

455 Justice, C., & Townshend, J. (2002). Special issue on the moderate resolution imaging
456 spectroradiometer (MODIS): a new generation of land surface monitoring. *Remote*
457 *sensing of environment*, 83(1), 1-2.

458

459 Kaufman, Y. J., Tanré, D., Remer, L. A., Vermote, E. F., Chu, A., & Holben, B. N.
460 (1997). Operational remote sensing of tropospheric aerosol over land from EOS moderate
461 resolution imaging spectroradiometer. *Journal of Geophysical Research: Atmospheres*
462 (1984–2012), 102(D14), 17051-17067.

463

464 Kotchenova, S. Y., Vermote, E. F., Matarrese, R., & Klemm Jr, F. J. (2006). Validation
465 of a vector version of the 6S radiative transfer code for atmospheric correction of satellite
466 data. Part I: Path radiance. *Applied optics*, 45(26), 6762-6774.

467

468 Kotchenova, S. Y., & Vermote, E. F. (2007). Validation of a vector version of the 6S
469 radiative transfer code for atmospheric correction of satellite data. Part II. Homogeneous
470 Lambertian and anisotropic surfaces. *Applied optics*, 46(20), 4455-4464.

471

472 Kotchenova, S. Y., Vermote, E. F., Levy, R., & Lyapustin, A. (2008). Radiative transfer
473 codes for atmospheric correction and aerosol retrieval: intercomparison study. *Applied
474 Optics*, 47(13), 2215-2226.

475

476 Levy, R. C., Remer, L. A., Mattoe, S., Vermote, E. F., & Kaufman, Y. J. (2007). Second
477 generation operational algorithm: Retrieval of aerosol properties over land from inversion
478 of Moderate Resolution Imaging Spectroradiometer spectral reflectance. *Journal of
479 Geophysical Research: Atmospheres* (1984–2012), 112(D13).

480

481 Masek, J.G., Vermote, E.F., Saleous, N.E., Wolfe, R., Hall, F.G., Huemmrich, K.F., Gao,
482 F., Kutler, J. & Lim, T.K., 2006. A Landsat surface reflectance dataset for North
483 America, 1990-2000. *Geoscience and Remote Sensing Letters*, IEEE, 3(1), pp.68-72.

484

485 Roy, D. P., Ju, J., Kline, K., Scaramuzza, P. L., Kovalskyy, V., Hansen, M., Loveland
486 T.R., Vermote E. & Zhang, C. (2010). Web-enabled Landsat Data (WELD): Landsat
487 ETM+ composited mosaics of the conterminous United States. *Remote Sensing of
488 Environment*, 114(1), 35-49.

489

490 Schaaf, C. B., et al. (2002), First operational BRDF, albedo nadir reflectance products
491 from MODIS, *Remote Sensing of Environment*, 83(1-2), 135-148.

492

493 Shuai, Y., Masek, J. G., Gao, F., & Schaaf, C. B. (2011). An algorithm for the retrieval of
494 30-m snow-free albedo from Landsat surface reflectance and MODIS BRDF. *Remote
495 Sensing of Environment*, 115(9), 2204-2216.

496

497 Tan, B., Masek, J.G., Wolfe, R., Gao, F., Huang, C., Vermote, E.F., Sexton, J.O. and
498 Ederer, G. (2013). Improved forest change detection with terrain illumination corrected
499 Landsat images. *Remote Sensing of Environment*, 136, pp.469-483.

500

501 Vermote, E.F., 2003, Adjacency effect. In *Encyclopedia of Optical Engineering*, pp. 39–
502 48 (New York: Marcel Decker).

503

504 Vermote, E.F., El Saleous, N., Justice, C.O., Kaufman, Y.J., Privette, J.L., Remer, L.,
505 Roger, J.C. & Tanre, D., 1997a. Atmospheric correction of visible to middle-infrared
506 EOS-MODIS data over land surfaces: Background, operational algorithm and validation.
507 *Journal of Geophysical Research*: (1984–2012), 102(D14), 17131-17141.

508

509 Vermote, E. F., Tanré, D., Deuze, J. L., Herman, M., & Morcette, J. J. (1997b). Second
510 simulation of the satellite signal in the solar spectrum, 6S: An overview. *Geoscience and
511 Remote Sensing*, IEEE Transactions on, 35(3), 675-686.

512

513 Vermote, E. F., & Saleous, M. N. (2006). Operational atmospheric correction of MODIS
514 visible to middle infrared land surface data in the case of an infinite Lambertian target. In
515 *Earth Science Satellite Remote Sensing* (pp. 123-153). Springer Berlin Heidelberg.

516

517 Vermote, E., Justice, C.O., Breon F.M., 2009. Towards a Generalized Approach for
518 Correction of the BRDF Effect in MODIS Directional Reflectances. *IEEE Transactions*
519 on Geoscience and Remote Sensing, 47(3), 898-908.

520

521 Vermote, E., Justice, C., & Csiszar, I. (2014). Early evaluation of the VIIRS calibration,
522 cloud mask and surface reflectance Earth data records. *Remote Sensing of Environment*,
523 148, 134-145.

524

525 **6. Tables caption**
526

527 **Table 1:** OLI surface reflectance APU scores expressed in 10^{-3} reflectance (compared to
528 TM and ETM+ surface reflectance APU by Claverie et al. (2015) over AERONET Site
529 and Ju et al., 2012 analysis for WELD and LEDAPS algorithm . Band number
530 corresponds to OLI band number designation and equivalent TM/ETM+ bands were
531 reported.

532 **Table 2:** OLI surface reflectance APU scores expressed in 10^{-3} reflectance (compared to
533 TM and ETM+ surface reflectance APU by Claverie et al. (2015) using Aqua MODIS
534 BRDF and spectrally adjusted surface reflectance CMG product as reference, the OLI
535 surface reflectance was aggregated over the CMG . Band number corresponds to OLI
536 band number designation and equivalent TM/ETM+ bands were reported.

538
539
540
541
542 **7. Figures caption**
543

544 **Figure 1:** Landsat 8/OLI RGB composite (Red Band 4, Green Band 3, Blue Band 2),
545 over Missoula, MT, acquired on June 30, 2013. The left side corresponds to the
546 reflectance at the top of the atmosphere, the right side to the surface reflectance. The
547 “color stretch” used for both sides is the same. The logarithm of the reflectance in each
548 band is scaled linearly between 5 (digital count 0) and 8.5 (Digital count 255).

549
550 **Figure 2:** Map of the ratio between MODIS Terra band 3 (0.47 μ m) and band 1
551 (0.67 μ m). This is the average ratio observed over a period of 10 years using coincident
552 MODIS/MISR observations and the optical thickness from MISR to perform atmospheric
553 correction.

554
555 **Figure 3a:** Flowchart of the Landsat8/OLI atmospheric correction scheme.

556
557 **Figure 3b:** Flowchart of the MODIS retrieval of the “Ratio” Map parameterized versus
558 NDWI at 0.05 degree.

559
560 **Figure 3c:** Flowchart of the OLI AOT retrieval.

561
562 **Figure 3d:** RGB detail of the Missoula scene (top left), (top right) color scaled residual:
563 the magenta pixels correspond to higher residual (Equation [5]) later flagged as cloud, the
564 red pixels were not flagged as cloud but discarded (in that case water and cloud shadow),
565 the purple pixels are clouds flagged early in the processing by the cirrus band (note the
566 threshold on the cirrus band has been set very conservatively ~ 0.02 reflectance unit).
567 (Bottom left) Cirrus band 9.

568
569 **Figure 4:** Comparison of the Accuracy, Precision and Uncertainty of the different surface
570 reflectance products in the red band, LEDAPS (Landsat 7/ETM+), WELD
571 (Landsat7/ETM+) using MODIS aerosol and Landsat8/OLI (this work). The reflectance
572 truth is obtained by correcting the TOA reflectance with 6SV using AERONET as input

573 for water vapor and aerosol. For reference also shown is the performance of the top of the
574 atmosphere data (same dataset as LEDAPS and WELD). The blue bars show the number
575 of point used in each bin of reflectance. The pink line represents the specified uncertainty
576 based on a theoretical error budget of the collection 5 MODIS surface reflectance. The
577 time period and sites used for Landsat8/OLI are different than the ones used for
578 LEDAPS, WELD and TOA datasets.

579
580
581 **Figure 5a:** Same as Figure 4 but for Landsat8/OLI band 1 (top left), 2 (Top right), 3
582 (Bottom left), 4 (Bottom right).

583
584 **Figure 5b:** Same as Figure 4 but for Landsat8/OLI band 5 (top left), 6 (Top right), 7
585 (Bottom left), NDVI (Bottom right).

586
587 **Figure 6:** Map of the AERONET sites (yellow squares) used for the validation and the
588 OLI scenes (red squares) used for the OLI-MODIS inter-comparison.

589
590 **Figure 7:** Cross-comparison between Aqua MODIS BRDF and spectrally adjusted SR
591 CMG product and OLI SR aggregated over the CMG. The five subplots correspond to
592 five OLI spectral bands used for the cross-comparison. Plots are represented through
593 density functions from light gray (minimum) to black (maximum); white means no data.
594 Red lines correspond to the linear fits. r^2 , A, P and U refer to the statistical metrics given
595 in Section 4. Relatives A, P and U are reported in parentheses. N is the number of points.

596
597 **Figure 8a:** Validation of Landsat (5/7) Albedo derived by Shuai et al. (2011) and Franch
598 et al. (2014). Note that Franch used AERONET data to improve the surface reflectance of
599 the LEDAPS reflectance product used as input. From Franch et al. 2014

600
601 **Figure 8b:** Same as Figure 8a but for Landsat8 Albedo, no AERONET data were used to
602 improve the surface reflectance product.

621
622
623

OLI Band	TM LEDAPS (Claverie et al., 2015)			ETM+ LEDAPS (Claverie et al., 2015)			ETM+ LEDAPS (Ju et al. 2012)			ETM+ WELD (Ju et al. 2012)			OLI This work		
	A	P	U	A	P	U	A	P	U	A	P	U	A	P	U
01													4.8	9.7	11.
02	3.7	5.7	6.8	6.7	7.7	10.	5.3	5.8	7.9	6.0	5.2	7.9	3.8	7.6	8.5
03	0.1	5.4	5.4	1.6	6.7	6.8	3.9	4.3	5.8	3.9	3.4	5.2	2.5	4.7	5.4
04	0.1	4.1	4.1	1.2	6.8	6.9	4.2	3.9	5.7	3.0	2.6	4.0	1.7	3.5	4.0
05	3.2	6.1	6.8	3.0	6.8	7.4	1.0	7.9	8.0	4.1	3.9	5.7	1.4	2.1	2.6
06	3.7	5.9	7.0	2.4	4.1	4.8	5.6	4.9	7.4	1.5	1.5	2.1	0.4	1.0	1.1
07	3.8	4.5	5.9	4.3	4.6	6.3	5.1	5.1	7.2	1.6	1.6	2.3	1.5	2.6	3.6

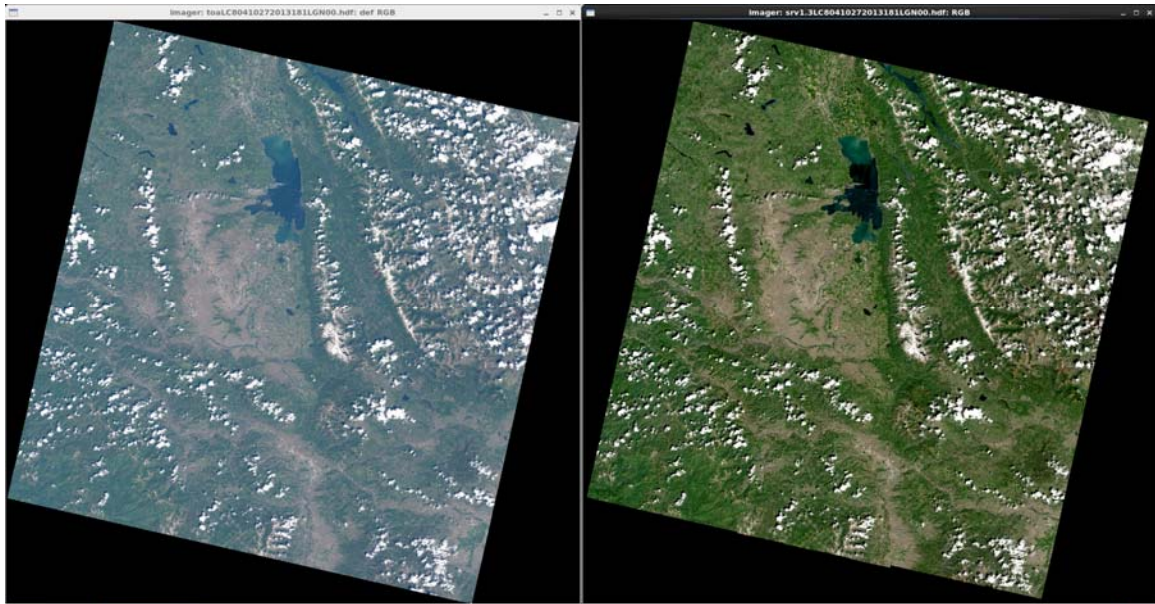
624 **Table 1:** OLI surface reflectance APU scores expressed in 10^{-3} reflectance (compared to
625 TM and ETM+ surface reflectance APU by Claverie et al. (2015) over AERONET Site
626 and Ju et al., 2012 analysis for WELD and LEDAPS algorithm . Band number
627 corresponds to OLI band number designation and equivalent TM/ETM+ bands were
628 reported.

629
630
631

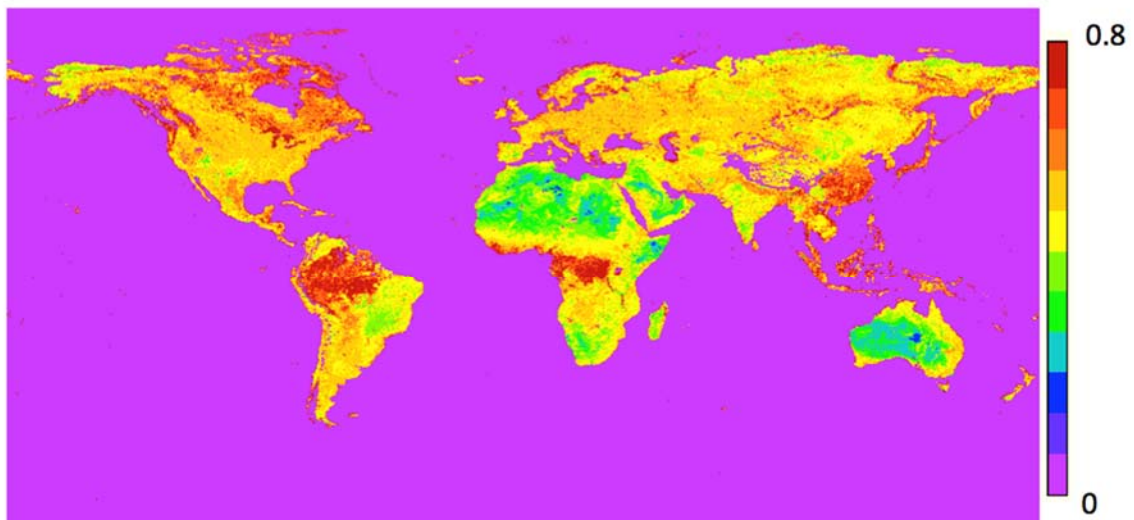
OLI Band	TM LEDAPS (Claverie et al., 2015)			ETM+ LEDAPS (Claverie et al., 2015)			OLI This work		
	A	P	U	A	P	U	A	P	U
2	7	9	11	9	7	12	2	6	6
3	1	9	9	6	9	11	3	6	7
4	9	10	14	1	9	9	1	6	6
5	5	17	17	3	14	15	2	12	12
7	1	14	14	5	15	16	9	11	14

632 **Table 2:** OLI surface reflectance APU scores expressed in 10^{-3} reflectance (compared to
633 TM and ETM+ surface reflectance APU by Claverie et al. (2015) using Aqua MODIS
634 BRDF and spectrally adjusted surface reflectance CMG product as reference, the OLI
635 surface reflectance was aggregated over the CMG . Band number corresponds to OLI
636 band number designation and equivalent TM/ETM+ bands were reported.

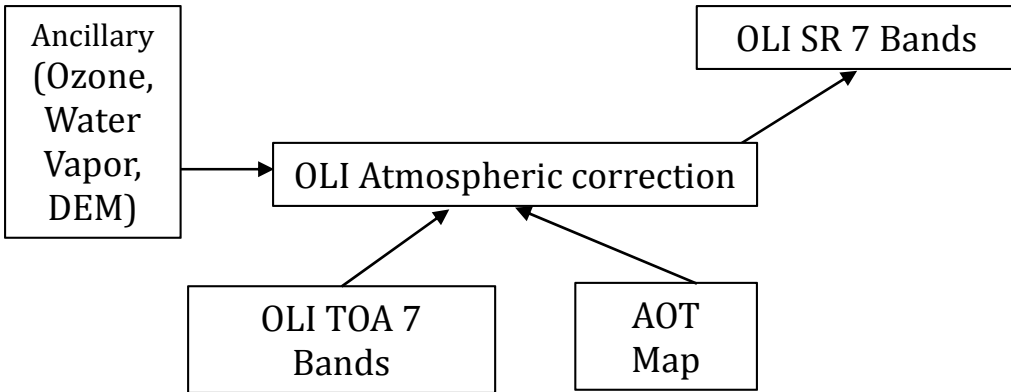
637
638
639



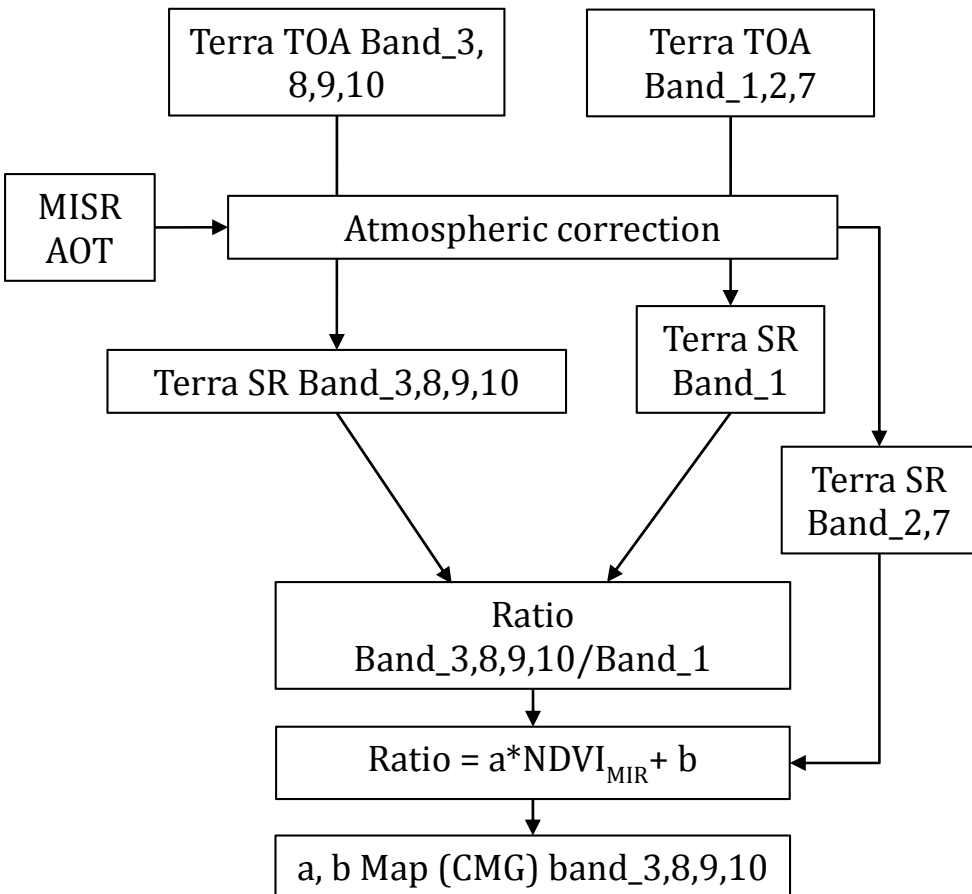
640
 641 **Figure 1:** Landsat 8/OLI RGB composite (Red Band04, Green Band03, Blue Band02),
 642 over Missoula, MT, acquired on June 30, 2013. The Left side corresponds to the
 643 reflectance at the top of the atmosphere, the right side to the surface reflectance. The
 644 “color stretch” used for both sides is the same. The logarithm of the reflectance in each
 645 band is scaled linearly between 5 (digital count 0) and 8.5 (Digital count 255).
 646
 647
 648
 649



650
 651 **Figure 2:** Map of the ratio between MODIS Terra band 3 (0.47 μ m) and band 1
 652 (0.67 μ m). This is the average ratio observed over a period of 10 years using coincident
 653 MODIS/MISR observations and the optical thickness from MISR to perform atmospheric
 654 correction.



655
 656
Figure 3a: Flowchart of the Landsat8/OLI atmospheric correction scheme.
 657
 658
 659
 660



661
 662
Figure 3b: Flowchart of the MODIS retrieval of the “Ratio” Map parameterized versus
 663 NDWI at 0.05 degree.
 664
 665
 666

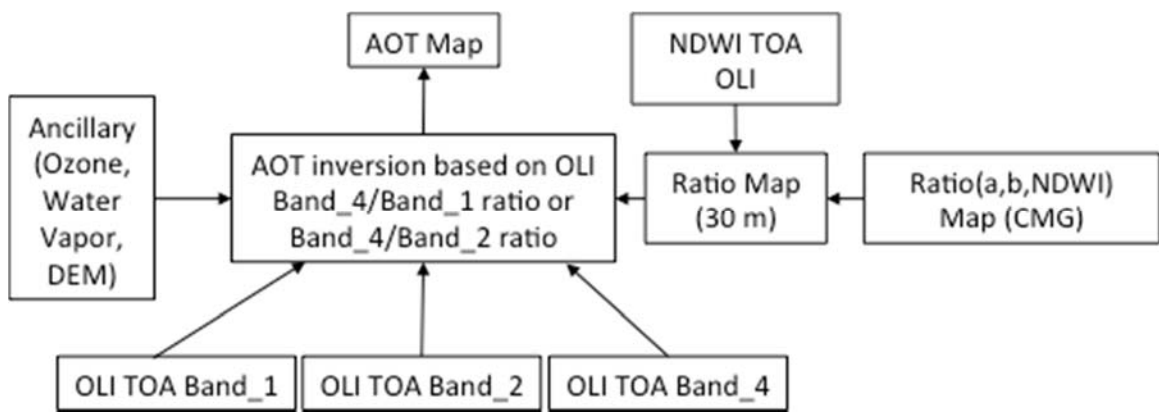
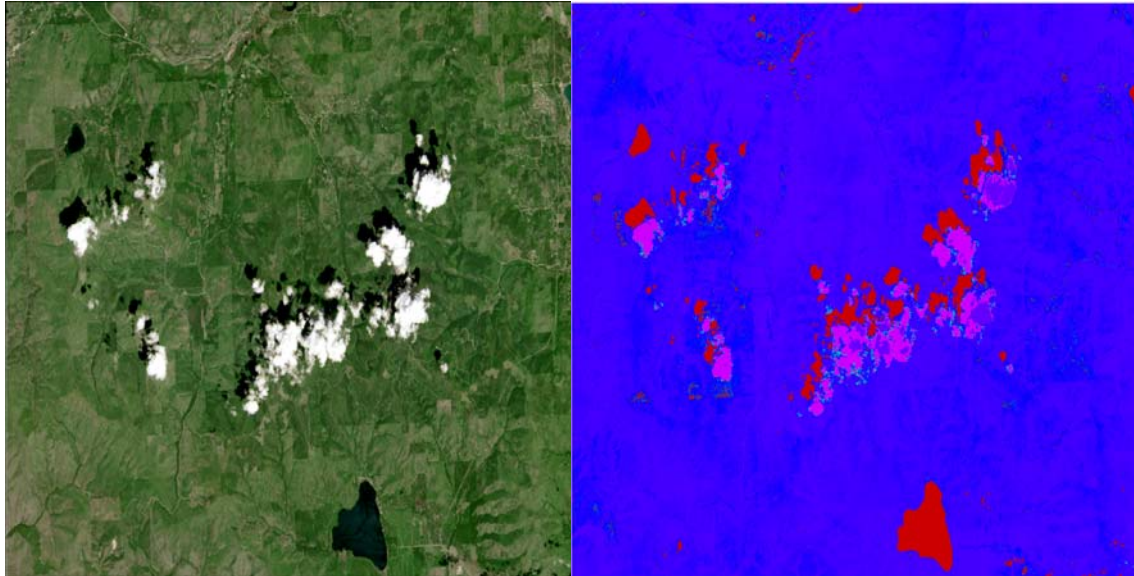


Figure 3c: Flowchart of the OLI AOT retrieval.

672
673



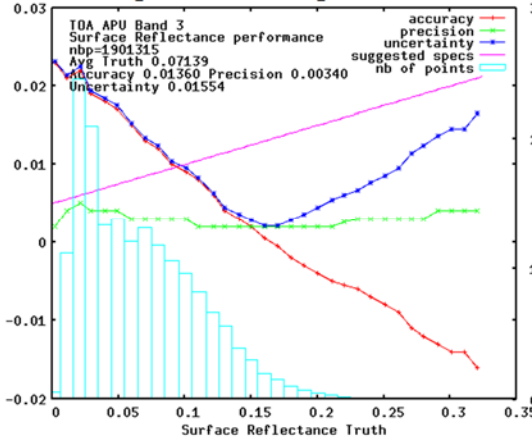
674

675
676

677 **Figure 3d:** RGB detail of the Missoula scene (top left), (top right) color scaled residual:
678 the magenta pixels correspond to higher residual (Equation [5]) later flagged as cloud, the
679 red pixels were not flagged as cloud but discarded (in that case water and cloud shadow),
680 the purple pixels are clouds flagged early in the processing by the cirrus band (note the
681 threshold on the cirrus band has been set very conservatively ~ 0.02 reflectance unit).
682 (Bottom left) Cirrus band 9.

683

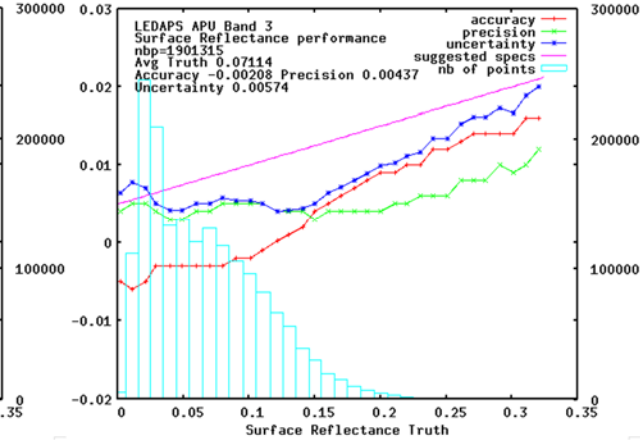
Top of the atmosphere



684

685

LEDAPS



686

687

688

Figure 4: Comparison of the Accuracy, Precision and Uncertainty of the different surface reflectance products in the red band, LEDAPS (Landsat7/ETM+), WELD (Landsat7/ETM+) using MODIS aerosol and Landsat8/OLI (this work). The reflectance truth is obtained by correcting the TOA reflectance with 6SV using AERONET as input for water vapor and aerosol. For reference also shown is the performance of the top of the atmosphere data (same dataset as LEDAPS and WELD). The blue bars show the number of point used in each bin of reflectance. The pink line represents the specified uncertainty based on a theoretical error budget of the collection 5 MODIS surface reflectance. The time period and sites used for Landsat8/OLI are different than the ones used for LEDAPS, WELD and TOA datasets.

689

690

691

692

693

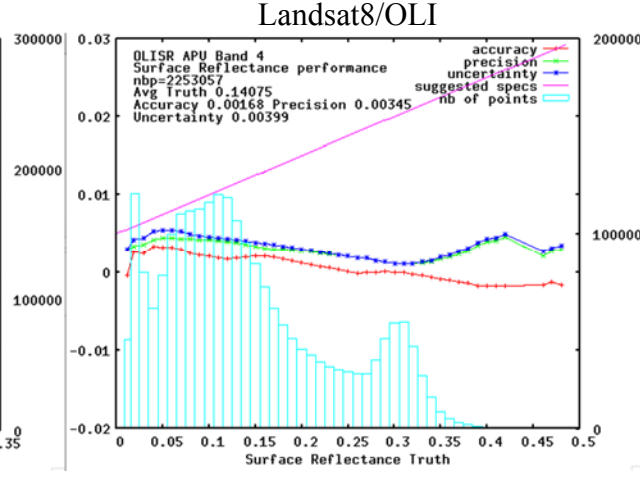
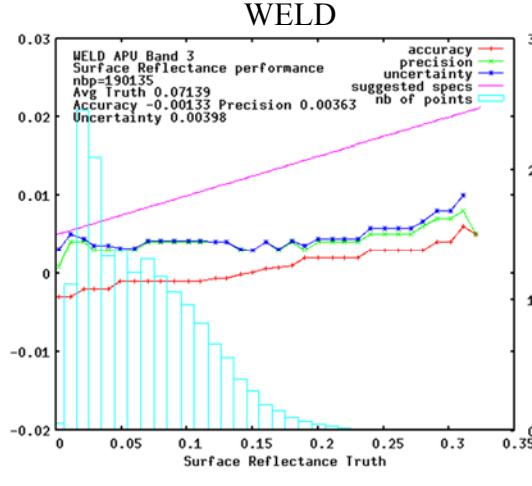
694

695

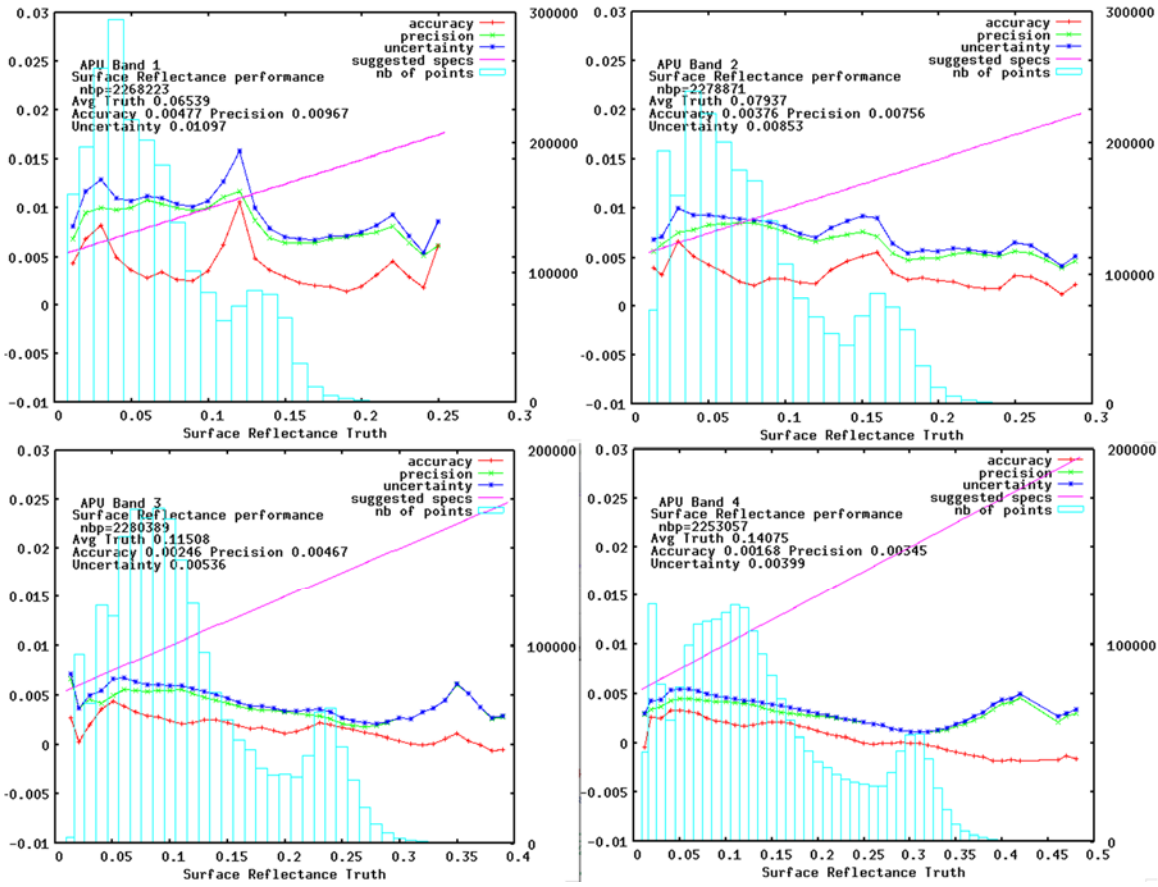
696

697

698



699



700

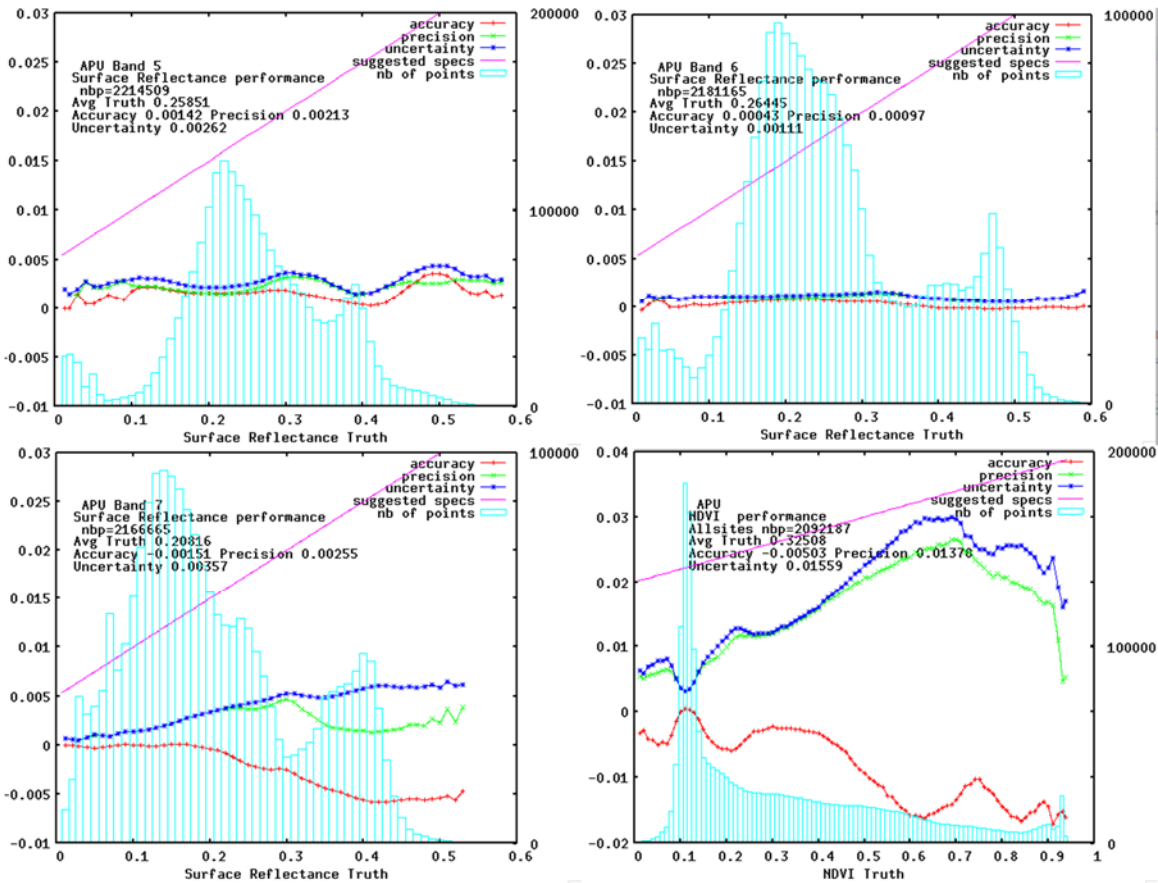
701

Figure 5a: Same as Figure 4 but for Landsat8/OLI band 1 (top left), 2 (Top right), 3 (Bottom left), 4 (Bottom right).

702

703

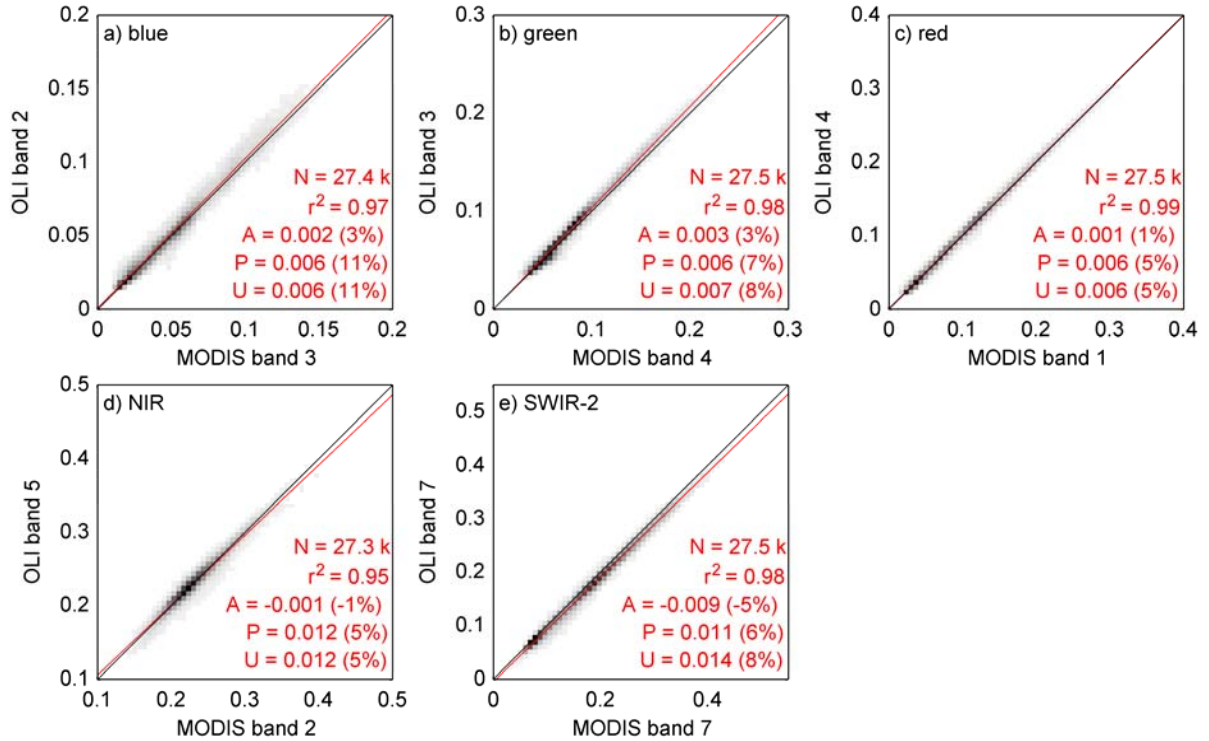
704



705
706 **Figure 5b:** Same as Figure 4 but for Landsat8/OLI band 5 (top left), 7
707 (Bottom left), NDVI (Bottom right).
708
709
710

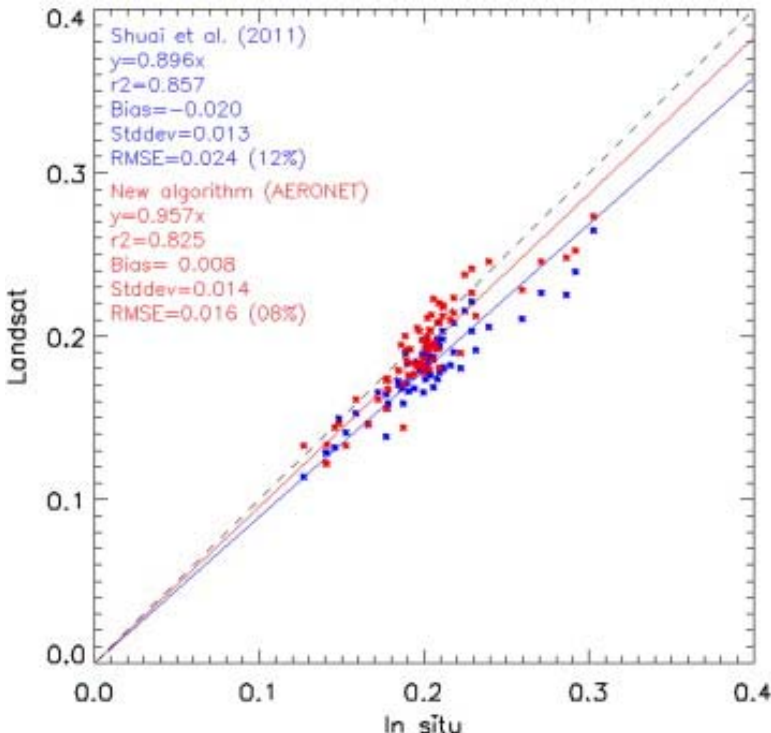


711
712 **Figure 6:** Map of the AERONET sites (yellow squares) used for the validation and the
713 OLI scenes (red squares) used for the OLI-MODIS inter-comparison.
714

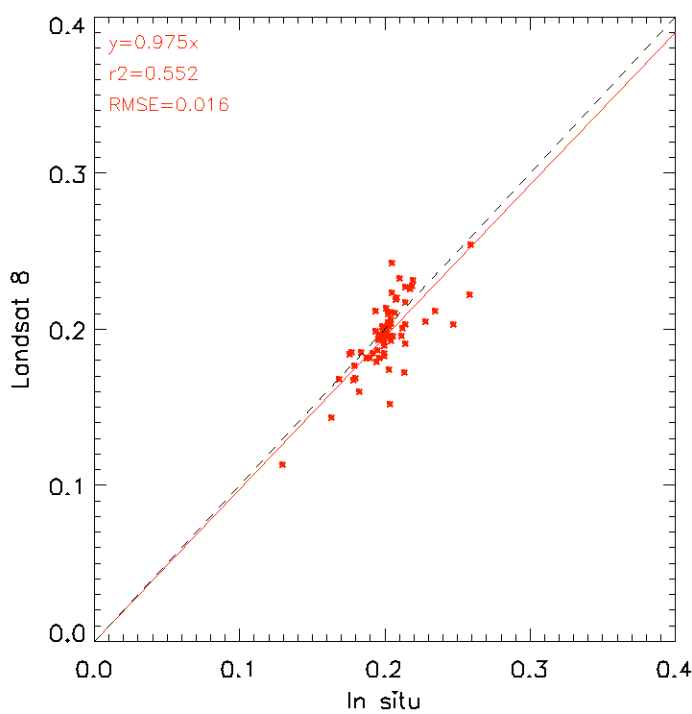


715
716

717 **Figure 7:** Cross-comparison between Aqua MODIS BRDF and spectrally adjusted SR
718 CMG product and OLI SR aggregated over the CMG. The five subplots correspond to
719 five OLI spectral bands used for the cross-comparison. Plots are represented through
720 density functions from light gray (minimum) to black (maximum); white means no data.
721 Red lines correspond to the linear fits. r^2 , A, P and U refer to the statistical metrics given
722 in Section 4. Relatives A, P and U are reported in parentheses. N is the number of points.



723
724 **Figure 8a:** Validation of Landsat (5/7) Albedo derived by Shuai et al. (2011) and Franch
725 et al. (2014). Note that Franch used AERONET data to improve the surface reflectance of
726 the LEDAPS reflectance product used as input. (From Franch et al. 2014.)
727



728
729 **Figure 8b:** Same as Figure 8a but for Landsat8 Albedo, no AERONET data were used to
730 improve the surface reflectance product.